Deep Convection and Column Water Vapor over Tropical Land vs. Tropical Ocean: A comparison between the Amazon and the Tropical Western Pacific

Kathleen A. Schiro[1] and J. David Neelin[1]
[1]Department of Atmospheric and Oceanic Sciences, University of California Los Angeles, Los Angeles, CA, USA

David K. Adams[2]
[2]Centro de Ciencias de la Atmósfera, Universidad Nacional Autónoma de México, México

Benjamin R. Lintner[3]
[3]Department of Environmental Sciences, Rutgers, The State University of New Jersey, New Brunswick, NJ, USA

Corresponding Author:
Kathleen A. Schiro
UCLA Department of Atmospheric and Oceanic Sciences
Math Sciences Building 7127
Los Angeles, CA 90095
Email: kschiro@atmos.ucla.edu
Phone: 845-527-6989

Abstract

The relationships between the onset of tropical deep convection, column water vapor (CWV), and other measures of conditional instability are analyzed with two years of data from the DOE Atmospheric Radiation Measurement (ARM) Mobile Facility in Manacapuru, Brazil as part of the GOAmazon campaign, and with 3.5 years of CWV derived from Global Positioning System meteorology at a nearby site in Manaus. Important features seen previously in observations over tropical oceans — precipitation conditionally averaged by CWV exhibiting a sharp pickup at high CWV, and the overall shape of the CWV distribution for both precipitating and non-precipitating points — are also found for this tropical continental region. The relationship between rainfall and CWV reflects the impact of lower free tropospheric moisture variability on convection. Specifically, CWV over land, as over ocean, is a proxy for the effect of free tropospheric moisture on conditional instability as indicated by entraining plume calculations from GOAmazon data. Given sufficient mixing in the lower troposphere, higher CWV generally results in progressively greater plume buoyancies through a deep convective layer. Although potentially greater sensitivity of buoyancy to boundary layer and microphysical processes is possible, the dependence on CWV is consistent with the observed onset of precipitation. Overall, leading aspects of the relationship between CWV and the transition to deep convection in the Amazon have close parallels over the tropical oceans. The relationship is robust to averaging on time and space scales appropriate for convective physics, but is strongly smoothed for averages greater than three hours or 2.5°.

1. Introduction

Despite the complex relationships, interactions, and feedbacks that exist among the atmosphere, land, and ocean, a robust relationship exists between precipitation and column water vapor (CWV). Bretherton et al. (2004) identified a smooth relationship of CWV and precipitation in daily mean satellite observations. On shorter timescales, conditionally average precipitation rate increases sharply with increasing CWV (Peters and Neelin 2006, Holloway and Neelin 2009, Neelin et al. 2009). This sharp pickup is associated with the onset of conditional instability leading to deep convection. Furthermore, statistics of the transition to deep convection are analogous to properties of a continuous phase transition at a critical value of CWV (Peters and Neelin 2006; Neelin et al. 2009) and can be understood in terms of stochastic variations across the deep convective onset threshold (Stechmann and Neelin 2011). Evaluating this deep convective transition using radiosondes from the DOE ARM site at Nauru in the tropical western Pacific, Holloway and Neelin (2009) demonstrated that CWV represents a proxy for the impact of free tropospheric humidity on the conditional instability of entraining plumes affecting the transition from shallow to deep convection, and thus that the statistics quantifying this transition provide a substantial constraint on subgrid scale processes that must be represented in climate models. It was previously unclear, however, the extent to which this simplifying CWV-precipitation relationship applies for convective transition statistics over tropical land, as fundamental differences exist in the convective environment over land compared to ocean - including a stronger diurnal cycle and greater variations in the boundary layer (Nesbitt and Zipser 2003).

There is substantial evidence suggesting the importance of free tropospheric humidity to the onset of deep convection (Austin 1948; Malkus 1954; Yoneyama and Fujitani 1995; Brown and Zhang 1997; Wei et al. 1998; Raymond and Torres 1998; Sherwood and Wahrlich 1999; Parsons et al. 2000; Raymond 2000; Raymond and Zeng 2000; Tompkins 2001a; Redelsperger et al. 2002; Ridout 2002; Bretherton et al. 2004; Chaboureau et al. 2004; Derbyshire et al. 2004; Grabowski 2003; Guichard et al. 2004; Sobel et al. 2004; Sherwood et al. 2004; Kuang and Bretherton 2006; Tian et al. 2006; Wu et al. 2009; Waite and Khouider 2010; Zhang and Klein 2010; Kumar et al. 2013), yet many models are currently too insensitive to free tropospheric humidity (Biasutti et al. 2006; Dai 2006; Oueslati and Bellon 2013). This insensitivity contributes to systematic errors and biases in simulated precipitation on a number of space and time scales: the erroneous appearance of a double inter-tropical convergence zone (Hirota and Takayabu 2013; Hirota et al. 2014); deficiencies in the simulation of the Madden-Julian Oscillation (Grabowski and Moncrieff 2004; Hannah and Maloney 2011; Jiang et al. 2011; Del Genio et al. 2011; Kim et al. 2012; Holloway et al. 2013; Kim et al. 2014; Rowe and Houze 2015); failure to represent the shallow-to-deep convective transition and diurnal cycle of deep convection (Randall et al. 1991; Yang and Slingo 2001; Betts and Jakob 2002; Dai and Trenberth 2004; Bechtold et al. 2004; Chaboureau et al. 2004; Guichard et al. 2004; Dai 2006; Del Genio and Wu 2010; Waite and Khouider 2010).The effect of free tropospheric humidity on the onset of deep convection can be explained through mixing between a convective plume and its surrounding environment, which greatly affects the plume's buoyancy. Mixing assumptions must, therefore, be appropriately constrained in convective parameterizations. This has been a long-standing challenge, yet several studies have demonstrated significant model improvement with realistic representations of entrainment processes (Neale et al. 2008; Bechtold et al. 2008; Zhao et al. 2009; Neelin et al. 2010; Sahany et al. 2012). In this regard, the convective transition statistics developed over tropical oceans have proven useful as model diagnostics (Sahany et al. 2012, 2014) that help to constrain entrainment representations, along with other observational and modeling studies (Raymond and Blyth 1986; Brown and Zhang 1997; Jensen and Del Genio 2006; Kuang and Bretherton 2006; Li et al. 2008; Bacmeister and Stephens 2010; Luo et al. 2010; Romps and Kuang 2010). The transition to deep convection can also be examined in the temporal domain (Holloway and Neelin 2010; Adams et al. 2013) in which timescales, lead-lag relations and the distinction between temporal onset and termination (Stechmann and Neelin 2014) can be important.

There are several additional variables and processes controlling the transition to deep convection that must also be understood and accurately represented in models: free tropospheric moistening processes (Johnson et al., 1999; Benedict and Randall, 2007; Kemball-Cook and Weare, 2001; Mapes et al., 2006; Hohenegger and Stevens 2013; Kumar et al. 2013; Masunaga 2013; Hagos et al. 2014); the influence of the diurnal cycle (Betts and Jakob 2002; Bechtold et al. 2004; Chaboureau et al. 2004; Del Genio and Wu 2010; Zhang and Klein 2010); the larger-scale dynamics forcing vertical ascent (Kumar et al. 2013; Hohenegger and Stevens 2013); convective downdrafts and cold pool formation (Tompkins 2001b; Khairoutdinov and Randall 2006; Schlemmer and Hohenegger 2014); cloud size (Boing et al. 2012); moist static energy gradients (Neelin and Held 1987; Raymond et al. 2003; Lintner and Neelin, 2007, 2008, 2010; Ma et al. 2011); vertical wind shear (i.e. Rotunno et al. 1988; LeMone et al. 1998); and microphysical processes, including cloud-aerosol interactions (Andreae et al. 2004; Khain et al. 2005). Important differences likely exist in the way these processes and variables contribute to the conditional instability of the environment over tropical land vs. tropical ocean.

Thus far, an insufficient observational record in the continental tropics has limited development of convective transition statistics, yet the Green Ocean Amazon campaign in Manacapuru, Brazil (2014-2015) has provided a unique opportunity to evaluate the transition to deep convection over land, to elucidate potential complexities compared to the ocean, and to develop simple, useful statistics as model diagnostics. Here, we derive the CWV-precipitation relationship and associated statistics with these data and with a complementary 3.5 year data set from the central Amazon using Global Positioning System (GPS) meteorology that provides continuous, all-weather observations of CWV at high temporal resolution over tropical land (Adams et al. 2011, 2013). Parallels are drawn between the land and the ocean to assess whether free tropospheric humidity is also of leading order importance to the conditional instability of an entraining plume over land as it is over ocean. The robustness of the convective transition statistics is tested as a function of spatial and temporal scales to establish a benchmark for comparison between models and observations at various scales. Lastly, the CWV-precipitation relationship is examined physically by linking vertical profiles of key thermodynamic quantities and plume buoyancies computed using turbulent mixing to the observed onset of deep convection.

2. Data

A suite of observations is used to establish relationships between CWV and deep convection across various instruments, time periods, and tropical locations. The principal location examined is the DOE ARM Mobile Facility at Manacapuru, BR (3° 12' S, 60° 35' W, 50 meters altitude), established as part of the GOAmazon field campaign (January 2014 - December 2015). The GOAmazon data used in this study cover the period 10 Jan 2014 to 20 Oct 2015. The results for the GOAmazon site are compared to those derived from two retired DOE ARM sites in the Tropical Western Pacific: Nauru Island (0° 31' S, 166° 54' E, 7 meters altitude) and Manus Island (2° 3' S, 147° 25' E, 4 meters altitude). The analysis period used in this study and in Holloway and Neelin (2009) for Nauru spans Apr. 2001- Aug. 2006, and the analysis period from Manus Island spans Jan. 2008 – Dec. 2010. In terms of radiosonde launches, these periods yield roughly comparable numbers to the western Pacific sites (3320 for Nauru and 3309 for Manus), each somewhat larger than the 2379 for GOAmazon.

Additional observations from a GPS meteorological station in Manaus, Brazil are included in this study; this station functioned from July 2008 to December 2011 as part of the National Oceanic and Atmospheric Administration/Earth System Research Laboratory (NOAA/ESRL) Real-Time Ground-Based GPS Meteorological Network and was located at the National Institute for Amazon Research/Large Scale Biosphere-Atmosphere Experiment (INPA/LBA) in Manaus (2.61°S, 60.21°W) (Adams et al. 2011, 2013).

a. Column Water Vapor

Radiosonde measurements at all ARM sites were obtained from Vaisala Digi-Cora III sounding systems at 2-second resolution; the raw sounding data were interpolated to 5-hPa intervals. Reported instrumental uncertainties are approximately 0.5^{o}C for temperature and 5% for relative humidity below 500 hPa. At the GOAmazon site, radiosonde launches occurred four times daily (6 hourly), at 05:30, 11:30, 17:30 and 23:30 UTC, with occasional launches at 14:30 UTC during the wet season. At Nauru, launches took place at 00:00 and 12:00 UTC, with occasional launches at 02:30 and 14:30 UTC, while at Manus Island, most launches took place at either 11:30 or 23:30 UTC, with occasional launches at 03:30 or 15:30 UTC.

CWV data sampled by microwave radiometer (MWR) at the GOAmazon site are derived from measurements of absolute microwave radiances (expressed as brightness temperatures) obtained at two frequencies: 23.8 and 31.4 GHz. The retrieval uncertainty for brightness temperatures is 0.3 K and for column water vapor is typically ~ 0.5 mm. All data for which the brightness temperature exceeds 100 K are removed from this dataset (Morris 2006), as are data that are affected by direct sunlight near local noon (15Z – 17Z) for roughly a 3-week period surrounding the equinoxes. To address the so-called wet-window problem, in which water collecting on the surface of the lens introduces measurement inaccuracy during rainy periods, we linearly interpolate CWV values across time-periods of 6 hours or less. While the linear interpolation procedure may introduce uncertainty (for example it likely underestimates peak CWV), the data gaps are typically short and the temporal persistence of water vapor values for strong convective events is on the order of hours (Holloway and Neelin 2010). Additionally, Figure A1 in the appendix illustrates that there is no obvious systematic bias at high CWV for the times sampled (15-minute average radiometer CWV surrounding radiosonde launch between 10 Jan 2014 and 30 Sep 2014), which suggests that this interpolation does not greatly affect the results presented in this study.

One way to overcome measurement inaccuracy during rainy times is through use of GPS technology, as its all-weather capability allows for CWV measurements during rainy times (Adams et al. 2011). The CWV from GPS is derived from water-vapor-induced delays in the radio signals from the satellite to the ground-based receiver (Bevis et al., 1992), and its accuracy in the Amazon is on the order of 1-2 mm (Adams et al. 2011). The INPA site consisted of a dual frequency, geodetic-grade GNSS receiver/antenna and meteorological station concurrently measuring pressure, temperature, relative humidity, winds, and precipitation at 1 min sampling frequency. NOAA/ESRL processed the GNSS data in near real time (2 h latency), with 30-minute average CWV values used in this study.

b. Precipitation

The GOAmazon precipitation measurements analyzed in Sections 3 and 4 are from the Aerosol Observing System (AOS) meteorological station, measured by the acoustic gauge of a Vaisala WXT520. When related to radiosonde CWV, AOSMET precipitation is averaged at 1-hour intervals surrounding the launch; for analyses with radiometer CWV, AOSMET precipitation is averaged at 15-minute intervals. In Section 3, the averaging intervals are varied to evaluate the robustness of the statistics. These data were chosen among many other datasets available because we deemed them the most reliable over the full 2014-2015 period (a detailed comparison of the different precipitation observing systems available at the GOAmazon site is included in the Appendix).

The precipitation measurements used in this study vary slightly across sites due to differences in instrumentation availability and reliability. In the tropical western Pacific at the Nauru and Manus Island ARM sites, precipitation was measured with an Optical Scientific optical rain gauge (ORG815), and 1-hour averages surrounding radiosonde launches are analyzed in Section 2. Section 5 uses precipitation from a Vaisala WXT-520 at the INPA site in Manaus, Brazil (30-minute averages) for the analysis with GPS-derived CWV.

Section 4 assesses the robustness of the statistics presented as the horizontal resolution of the precipitation measurements decreases. We thus average precipitation from the Tropical Rainfall Measuring Mission's (TRMM) 3B42 (version 7) product across various spatial scales. The 3B42 precipitation estimates (mm hr^{-1}) have a 3-hourly temporal resolution on a $0.25^o \times 0.25^o$ grid, covering 50^oS - 50^oN from 01 Jan 1998 - present. The TRMM 3B42 precipitation estimates are a combination of multiple independent precipitation estimates from various microwave retrievals and algorithms, while missing data in individual 3-hourly merged-microwave retrievals are filled with microwave-adjusted merged geo-infrared (IR) estimates. The precipitation radar (PR) and TRMM microwave imager (TMI) are used to calibrate all input microwave data, while the IR estimates are computed using monthly matched microwave-IR histogram matching (Huffman et al. 2007). Estimates of precipitation from the microwave instruments are derived from several versions of the Goddard Profiling Algorithm (GPROF), a multi-channel physical approach used to retrieve rainfall and vertical structure information (Kummerow et al. 2001). Over the oceans, GPROF uses signals from emission at low frequencies and scattering at higher frequencies. Over land, the algorithm reduces to a scattering-type procedure using only the higher-frequency channels. All of these estimates are adjusted to a best estimate using probability matching of precipitation rate histograms assembled from coincident data. Note that both the microwave and IR data are snapshots, except for small regions in which two or more overlapping microwave scenes are averaged. Generally, however, each satellite provides a sparse sampling of precipitation. As a result there can be significant gaps in the 3-hourly coverage by passive microwave estimates. Because of this, precipitation estimates can be thought of as instantaneous values, representative of the 3-hour period in which they fall.

3. The Relationship between Deep Convection and CWV over Tropical Land vs. Tropical Oceans

a. The GOAmazon Site - Manacapuru, BR

To illustrate the relationship between CWV and deep convection at the GOAmazon site, we conditionally average precipitation rate by CWV in Figure 1. Figure 1a is the 1-hour average precipitation rate conditioned on radiosonde CWV, with the average centered at the time of radiosonde launch. Measurements for all available times (05:30, 11:30, 17:30 and 23:30 UTC, and occasionally 14:30 UTC) were included in the averages. Note that for the statistics presented throughout, CWV bins are typically of equal 1.5 mm width and range from 28 mm to 70 mm; exceptions to this will be noted where appropriate, such as here, where the highest CWV bin spans 6 mm from 64 mm to 70 mm, in order to include sufficient counts.

Beyond a threshold CWV value, a sharp increase in rain rate is evident. This confirms that the CWV-precipitation relationship and associated behavior exists over tropical land as it does over tropical ocean (Peters and Neelin 2006; Neelin et al. 2009; Holloway and Neelin 2009). The limited sampling of high CWV in the GOAmazon radiosonde observations, reflected in the large error bars (+/- 1 standard error), limits the precision with which the behavior above the pickup can be estimated; nevertheless, the data are sufficient to establish the occurrence of the pickup, and the radiosonde observations are key to analyzing the vertical structure, which will be discussed in Section 6 below.

The larger sample size of radiometer CWV affords better quantification of the behavior at high CWV (Figure 1d). For this purpose, Figs. 1d-f include four additional 1.5 mm bins at high CWV, in comparison to Figs. 1a-c. A sharp pickup is clearly evident in this dataset. Additionally, the conditionally averaged rain rates in the 61-64 mm range in Fig. 1a and the magnitudes observed in the 61-64 mm range of Fig. 1b mimic each other, demonstrating the robustness of the results across various instruments. A strong correlation (r=0.91) between the 15-minute average radiometer CWV and radiosonde CWV (see Fig. A1) further highlights this consistency.

The value of CWV at which the rapid pickup in precipitation begins, referred to as the critical value, is a useful measure in characterizing this onset. For the short, *in situ* datasets used here, empirical fits involve relatively few points with large error bars, so we simply use the point at the beginning of the rapidly increasing range as a rule of thumb. Estimating the critical value by a linear fit through the range over which precipitation is rapidly increasing, as in Sahany et al. 2014, and choosing a range of above 1 mm hr^{-1} (appropriate for these data) yields a CWV value of ~60mm where the interpolation crosses 1 mm hr^{-1} (Fig. 1d). This range is, however, instrument dependent.

Compared to the results from Neelin et al. 2009, the mean tropospheric temperature at the GOAmazon site is 271.4 K, so the location of the pickup for GOAmazon occurs at lower CWV (~ 61 mm) than for comparable temperatures in the tropical eastern Pacific (~ 65 mm, interpolated between 271 and 272 K). This is consistent with the expectation that the mean tropospheric temperature is only one of several controls on the onset of conditional instability and thus the location of the pickup, and indicates that other key factors differing between tropical land and ocean are reflected in the onset. Specifically, boundary layer dynamics introduce additional complexity to the transition to deep convection over land, as the diurnal cycle is stronger over land and the partitioning of surface net radiation between latent and sensible heat fluxes depends on the interactions between several surface attributes (e.g., vegetation growth and soil moisture) and the atmosphere.

The curvature above the critical CWV in the radiometer analysis is qualitatively resembles the behavior observed over the tropical oceans (Peters and Neelin 2006; Neelin et al. 2009), but we are cautious in drawing conclusions about this given the scatter at high values and limitations of the radiometer. The quantitative values of the conditionally averaged precipitation in the pickup region are slightly smaller than those in microwave retrievals in Neelin et al. (2009) and Sahany et al. (2014), presumably in part a result of inherent uncertainties at high rain rates, particularly in the satellite observations where precipitation is inferred from cloud liquid water. Comparing the 15-minute averages from the GOAmazon site to microwave retrievals over the tropical oceans (effectively snapshots) may also play a role.

Figures 1b and 1e illustrate an equally sharp increase in probability of precipitation as a function of CWV comparable to that shown for conditionally averaged rain rate in Figs. 1a and 1d, respectively. The fraction of precipitating points per CWV bin is defined as the number of CWV observations with rain rates greater than a small threshold (here 0.5 mm hr^{-1}), divided by the total number of CWV samples in each bin. The probability increases dramatically above the critical value, sharply increasing to values greater than 50% in the highest CWV bins.

Figures 1c and 1f show the frequency of occurrence of different CWV values for all times and for precipitating times (where precipitation rates exceed 0.5 mm hr^{-1}) at the GOAmazon site for radiosonde and radiometer CWV, respectively. Curves are scaled with respect to CWV bin sizes, similar to a probability density function (PDF) but in counts per millimeter - referred to here as frequency density. We chose not to normalize to instead yield PDFs to make the counts for each bin visible, as the lengths of the available datasets vary by instrument and location. The peak in the distribution of CWV, for both the radiometer and radiosonde analysis, occurs between 55-60 mm. The occurrence of the peak in the distribution occurs just below the critical point, consistent with the findings of Peters and Neelin (2006) and Neelin et al. (2009). The highest probability state of the system is near the beginning of the intense precipitation regime, as is shown by the distribution of precipitating points (the peak occurs in the 61-62.5 mm bin in the radiometer analysis, and is slightly more spread out in the radiosonde data). Below 45 mm, no events exceeding the 0.5 mm hr^{-1} threshold are observed.

The longer-than-Gaussian tails of this distribution are also consistent with those seen in previous studies (Neelin et al. 2009; Neelin et al. 2010), seen here with different instrumentation. Because of the lower number of radiosonde observations, we focus on radiometer observations (Fig. 1f). Firstly, there is a long tail extending towards lower CWV in the distribution for precipitating points. The peak occurs just below or near the critical point, with a sharp decrease in frequency towards higher CWV in the region of rapid pickup of precipitation, consistent with the dissipative effects of precipitation on CWV (and of convection on buoyancy). Beyond the critical value, there is evidence of a long tail with roughly exponential decay as CWV increases, suggesting that the system is characterized by a higher frequency of extremes than would be expected from Gaussian statistics. This behavior is particularly evident in the radiometer analysis shown in Fig. 1f, but low counts in the high CWV bins limit confidence in this feature.

Many of the transition to deep convection statistics can be qualitatively and quantitatively captured by a simple stochastic model (Stechmann and Neelin 2011). This model suggests that the long tail for precipitating points in the low CWV regime is associated with a transition probability in which it typically takes some time to transition to a non-raining state when CWV decreases from the raining regime. The same hysteresis affects the position and value of the peak in the distribution for precipitating points, consistent with results here, suggesting it may be interesting in further work to distinguish temporal aspects of the transition, including formation of stratiform rain. The behavior of the distribution for all points at low CWV is expected to be rather dependent on the dynamics of the dry regime and has been noted to have various forms over ocean basins, including a second maximum. This may occur near the balance between evaporation and moisture divergence (Lintner and Neelin 2009).

We suggest that the statistics presented here provide useful observational constraints for representing the transition to deep convection in stochastic convective parameterizations, and shed some light on important differences between land and ocean that must be considered.

b. The Tropical Western Pacific

Figure 2 illustrates the CWV-precipitation relationship for two sites in the tropical Western Pacific - Nauru (Fig. 2a-c) and Manus Island (Fig. 2d-f). Compared to the Amazon in Fig. 1, the tropical western Pacific sites show very similar behavior. Radiosonde estimates are shown in Fig. 2, which can be directly compared to Fig. 1a-c. Both pickups of precipitation, for Nauru (Fig. 1a) and Manus Island (Fig. 1d), occur at higher values of CWV (~67 mm) than in the Amazon. As was discussed in Section 1a, this is due in part to small differences in the mean tropospheric temperatures (272.0 K at Nauru, 271.9 K at Manus Island) but is also likely due to key fundamental differences in the convective environments of a tropical land site vs. a tropical oceanic site. For reference, the values of column integrated saturation specific humidity ($\widehat{q_{sat}}$) for the three sites are 76.0 mm, 75.2, and 73.0 mm at Nauru, Manus Island and the GOAmazon site, respectively, although it is known for tropical ocean basins spanning a wider range of tropospheric temperatures that $\widehat{q_{sat}}$ poorly captures the temperature dependence (Neelin et al. 2009, Sahany et al. 2012) because the relevant physical control is conditional instability rather than large-scale saturation.

As in the GOAmazon case, the fractions of precipitating points (Figs. 2b and 2f, for Manus Island and Nauru respectively) sharply increase to 50% or greater beyond a critical CWV. This, again, illustrates that a sharp transition occurs not only in rain rate, but also in the probability of precipitation beyond a threshold CWV. In Fig. 2c, Manus Island exhibits distinct peaks in its distributions: the peak of the CWV distribution occurs between 58 and 60 mm, whereas the peak in the distribution of precipitating points occurs between 60-63 mm. This is consistent with the findings from previous studies, where the peak in the precipitating points occurs at slightly lower CWV than the critical value. Also consistent is the sharp decrease in the frequency of CWV between the distribution peak and the CWV values where precipitation picks up rapidly. These characteristics are also observed for Nauru, but the peaks in the distributions of CWV and the precipitating points are broader in this sample from radiosondes, i.e., the CWV distribution peak spans roughly 8 mm (~50-58 mm), whereas the peak in the distribution of precipitating points spans roughly 10 mm (~57-67 mm).

Even though marginal differences can be observed across locations, the main features of these statistics are consistent and robust across all three tropical locations. This suggests that CWV is a good proxy for conditional instability and has a clear relationship to the onset of deep convection throughout the tropics.

4. The robustness of the observed statistics at various scales

a. The effects of temporal averaging

To explore how averaging over differing temporal scales can affect the statistics describing the transition to deep convection, we compute the transition statistics at various averaging intervals with *in situ* precipitation and radiometer CWV from the GOAmazon site. Four averaging intervals were chosen for this analysis: 15-min, 1-hour, 3-hour and 1-day averages. These intervals were chosen to be most comparable to the current output available from models and observations.

In Fig. 3a, the magnitude of the conditionally averaged precipitation in the highest four CWV bins diminishes considerably as the averaging interval increases. For 3-hour averages, the pickup is degraded, while for daily averages, the pickup is almost non-existent. Despite some variability in the shapes of the curves, the overall locations of the pickups are robust for temporal resolutions of three hours or less. The location of the probability curve pickup, however, varies substantially as the size of the averaging interval increases: larger averages pick up sooner and have a higher probability of precipitating at high CWV. This can be explained by the fact that the 3-hourly and daily averages are more likely to span times where it is raining than the shorter averages are. Overall, these results illustrate how the statistics vary with temporal resolution, which should be considered when applying them as model diagnostics.

b. The effects of spatial averaging

The relationship between spatially averaged TRMM 3B42 3-hourly instantaneous precipitation (see Section 2) and radiometer CWV (15-min averages) over the GOAmazon site is shown in Figure 4 for 0.25 x 0.25 degrees (a-c), 1.25 x 1.25 degrees (d-f), and 2.5 x 2.5 degrees (g-i). At either 0.25^{o} or 1.25^{o}, the relationship is comparable to the results in Fig. 1 and thus robust. However, at 2.5^{o}, it starts to deteriorate, as the pickup of precipitation and the percentage of precipitating points occur too soon in comparison to Fig. 1d-e. These results are encouraging, as they suggest that resolutions up to about 1.25 x 1.25° are still of sufficient spatial resolution to reproduce robust statistics that explain the CWV-precipitation relationship, given that the temporal resolution is also adequate. This implies that these statistics are reproducible using the horizontal resolutions available with many current generation GCMs. In such comparisons, it should be borne in mind that a GCM with, e.g., 2° resolution may respond at the finest scale available to it, i.e. the grid scale, in a manner similar to the convective response occurring at finer scales in observations.

5. Use of GNSS Meteorological Networks in the Tropics

For two decades, GNSS/GPS meteorology has offered relatively inexpensive, high-frequency (~5 min), all-weather retrievals of CWV, and is thus ideal for analyses requiring long, continuous records of observed CWV over land. This is particularly useful for studies in the tropics, where collecting in-situ measurements is a challenge. We thus evaluate the convective transition statistics here for GPS data from a site near Manaus. In Figure 5, the statistics are reproduced for GPS CWV and coincident measurements of precipitation (30-

minute averages) as in Fig. 1. Note that the precipitation measurements from the INPA site are biased low (see Appendix). Therefore, for better comparison to the statistics in Fig. 1, the range shown on the precipitation axis (0-1.28 mm hr^{-1}) is reduced relative to the range on the other pickup plots (0-6 mm) by a factor of 4.7 - the ratio of means of precipitating points between the 30-minute average precipitation from both sites. Additionally, the threshold for identifying precipitating points is lowered to 0.1 mm hr^{-1} to more appropriately complement the 0.5 mm hr^{-1} threshold used in Fig. 1. When measurement differences are properly accounted for, Figs. 1 and 5 compare well: the location and shape of the pickup of precipitation is consistent, the probability of precipitation is just below 50% in the highest bin, and the distribution of CWV and precipitating points resides near to the transition, with a sharp drop in frequency between the peak and the transition and a long tail extending out to high CWV. This suggests GPS technology will be valuable in observing characteristics of convection at high temporal resolution throughout tropical land regions.

6. Characterizing the variability of column moisture

a. Vertical thermodynamic profiles

Vertical profiles of thermodynamic quantities - specific humidity (q), relative humidity (RH) and equivalent potential temperature (θ_e) - are conditionally averaged on CWV in Figs. 6a, 6b, and 6c, respectively. In Fig. 6a, it is evident that profiles of q are most variable in the layers above 800 mb at the GOAmazon site. This differs slightly from the western Pacific case, as the variability in free tropospheric q (850-500mb) with respect to CWV is slightly less over the Amazon than it is for Nauru (see Figure 3a Holloway and Neelin 2009), presumably due to stronger horizontal moisture gradients near Nauru. Additionally, the contribution from the boundary layer is greater at the GOAmazon site than it is over the tropical western Pacific.

RH profiles belonging to the highest CWV bins at the GOAmazon site (> 61 mm) are at least 90% saturated throughout the lower troposphere. At Nauru, this is the case for CWV greater than 66 mm (see Fig. 4a, Holloway and Neelin 2009), suggesting that the column is saturated for lower CWV in the Amazon than it is over the tropical western Pacific. The variability observed in RH is highly consistent with variability in column moisture, since free tropospheric temperature variations tend to be modest.

Equivalent potential temperature (θ_e), calculated reversibly following Emanuel (1994) in Fig. 6c, is an approximate measure of non-entraining parcel buoyancy, as convective available potential energy (CAPE) can be approximated by drawing a vertical line upward from the initial θ_e. Where this line crosses the θ_{es} curve is roughly the level of free convection (LFC) of the unmixed parcel; the area to the left of the vertical line and to the right of the θ_{es} curve is roughly proportional to CAPE. θ_e at the GOAmazon site shows similar overall variability in the vertical as it does at Nauru. In the absence of entrainment, many of the profiles belonging to the highest CWV bins have sufficient θ_e to support deep convection, providing that the convective inhibition (CIN) residual from the nighttime hours (seen in the θ_e profile) could potentially be overcome. This will be discussed further in Section 7.

b. Moisture anomalies

Figure 7 illustrates the differences in q at 1.5 - 3 hours leading (red) and 1.5 - 3 hours lagging (blue) precipitation, between profiles corresponding to precipitation events (rain rate > 0.5 mm hr^{-1}) and those that do not correspond to a precipitation event (rain rate < 0.01 mm hr^{-1}) for January - April soundings only. Leading an event, moisture anomalies exceeding 0.5 g kg^{-1} and as large as 1 g kg^{-1} are seen clearly throughout the lower troposphere. This is consistent with evidence that increased low-tropospheric humidity supports deep convective initiation. These moisture anomalies are also seen in the tropical western Pacific at Nauru (Fig. 5, Holloway and Neelin 2009), where anomalies as large as 3 g kg^{-1} occur in the lower-mid troposphere within 3 hours of a precipitation event.

Within 1.5 hours before the precipitation event, the anomaly increases throughout the entire troposphere, with a particularly large increase in the lower troposphere between 750-950 mb, highlighting the enhancement of moisture in the lower troposphere as playing a role in the onset of deep convection. During a precipitation event, the anomaly in the 750-950 mb layer decreases, suggesting that moist air is lofted by updrafts, with drier air from downdrafts diluting the layer's moisture content. This lofting and detrainment of moist air can be seen in the increased anomaly of mid-upper tropospheric humidity between 200-700 mb. As precipitation dissipates, this mid-upper tropospheric anomaly persists for hours afterwards, which may aid in supporting subsequent convective events. These anomalies are present in the tropical western Pacific case as well, but the vertical structure is more consistent throughout the 6-hour period than it is for the GOAmazon case, i.e. the maximum q anomaly at all times is around 800 mb. In the GOAmazon case, on the other hand, the maximum 1.5 hours before precipitation is found around 900 mb, during precipitation it is around 700 mb, and after precipitation it is found at about 500 mb. Additionally, separating the analysis out by time-of-day (not shown) indicates that these moisture anomalies are consistent for events occurring at all times of day.

Overall, in both the Amazon and the tropical western Pacific, humidity is enhanced throughout most of the troposphere for several hours leading and lagging the original precipitation event. Free tropospheric humidity appears to behave similarly in land and ocean cases (although with larger amplitude variation in the Western Pacific), whereas boundary layer moisture is more variable on short time scales in the land case. The Amazon also more clearly exhibits lofting of moisture into the upper tropospheric moisture, while both the Amazon and western Pacific exhibit reduced boundary layer moisture after convection.

c. Dependence on Time-of-Day

Considering the strength of the diurnal cycle over land, it is natural to wonder whether CWV is a good proxy for conditional instability at all times of day, given how conditions contributing to instability can vary diurnally. Fig. 8

suggests that the relationship between CWV and precipitation is robust at all times of day. Figure 8a shows the relationship between 15-min average radiometer CWV and precipitation for nighttime hours (7 pm – 8 am). The time intervals were chosen to complement the radiosonde launch times and the analysis presented in Section 7. Figure 8d shows this relationship for the midday hours, which are the most convective hours of the day (10 am – 4 pm). The pickups of both conditionally averaged precipitation (Figs. 8a and 8d) and the probability of precipitation (Figs. 8b and 8e) affirm that the relationship is robust throughout all times of day. The frequencies of occurrence of precipitation (Figs. 8c and 8f) are also consistent with the results in Fig. 1. Despite the fact that more convection occurs in the midday hours over the Amazon, the relationship holds true for all times of day.

7. The sensitivity of plume buoyancy to entrainment under simple freezing assumptions

In this section we focus on connecting the observed pickup of precipitation to observed increases in buoyancy and the sensitivity to entrainment. We calculate the buoyancy perturbation profiles, the virtual temperature difference between the environment and the plume $\left(\Delta T_v = T_{V,plume} - T_{v,env}\right)$ for plumes rising from the subcloud layer (1000 hPa), with mixing occurring at each pressure level as described by

$$r_k = (1 - x_{k-1})r_{k-1} + X_{k-1}\tilde{r}_{k-1} \qquad \textbf{(1)}$$

where X is the mixing coefficient, r is a conserved variable (with $\tilde{r}$ its environmental value), and k denotes pressure level if X varies. Here we calculate the mixing coefficient proportional to z^{-1}, where z is height, in the layer in which plume mass flux is growing. This mixing assumption was referred to in Holloway and Neelin (2009) as Deep Inflow A (DIA) and corresponds to the Siebesma et al. (2007) LES-based dependence. DIA is chosen here because of its realistic representation of buoyancy perturbation profiles and overall consistency with the pickup of precipitation observed in Fig. 1, and is described as

$$X_k = c_{\in} z_k^{-1} \Delta z \qquad \textbf{(2)}$$

where X_k is the coefficient in (1), Δz is a positive finite difference layer depth, and $c_{\in}$ = 0.4. Following Holloway and Neelin (2009), a simplified limiting case of freezing microphysics is also used: all condensate is conserved and freezing is assumed to take place very rapidly when the parcel reaches the freezing level.

The individual perturbation profiles are shown in Figure 9 and have been conditionally averaged by CWV, with bin spacing as in Fig. 1a. Figure 9a illustrates the profiles of the radiosondes from all times of day, which exhibits a distinct layer of CIN between the surface and 800-850 hPa. It is evident that only the highest CWV bins could be deep convective, but when averaging the profiles over all times of day it appears that even the profiles belonging to the highest CWV bins would struggle to become deep convective. Since the afternoon is the most convective time of day in the Amazon (Machado et al. 2004), we also separate the profiles by time-of-day to examine key thermodynamic differences and how stability in the nighttime hours could be contributing to the CIN observed in Fig. 6a.

Figure 9b, which includes nighttime soundings only (05:30, 11:30 and 23:30 UTC), shows the large layer of CIN seen in Fig. 9a; this shows that the CIN is unique to the nighttime soundings and implies that the CIN is largely present as a result of radiative cooling. At these times of day, it is unlikely for convection to fire as a result of local instability, which is consistent with the buoyancy profiles in Fig. 9b. In Figure 9c, only profiles from late morning (14:30 UTC) and early afternoon (17:30 UTC) soundings were conditionally averaged by CWV. In contrast to the evening/morning soundings, there is very little CIN. The variability observed in the upper CWV bins is due to the low counts of profiles contributing to the average. Overall, it appears that a variety of CWV values would be conducive to convective activity in the afternoon hours, with CWV bins < 60 mm acting to support shallow convection, whereas only the highest CWV bins act to support deep convection.

Some caveats on this analysis should be noted:

(1) The plume buoyancies sorted by CWV are considerably smaller in the lower troposphere compared to the tropical western Pacific case for the same computation (Holloway and Neelin 2009, Fig 8c). The onset of deep convection is thus likely dependent upon other factors unique to tropical land cases, in particular the greater variability of the boundary layer. Additionally, there are key thermodynamic differences between the convective environments in the wet and dry seasons in the Amazon and thus likely differing thermodynamic controls on deep convection; i.e. during the wet season, there is less CIN, less CAPE and more moisture available throughout the column, whereas in the dry season there is more CIN, more CAPE and less moisture available in the column (Collow et al. 2016).

(2) Entrainment assumptions can affect the details of the buoyancy profiles seen in Fig. 9c. In particular, smaller/larger values of the mixing coefficient in the lower troposphere yield larger/smaller buoyancy values. More complex entrainment assumptions would obviously also have impact, e.g., the entrainment rate weakening as convection over land deepens (Del Genio and Wu 2010; Stirling and Stratton 2012), having a parameterized dependence on environmental humidity (Zhang and Klein 2010; Stirling and Stratton 2012) or a dependence on cloud size (Simpson 1971; Grabowski 2006; Khairoutdinov and Randall 2006; Stirling and Stratton 2012). However, the computations here indicate a strong dependence on free tropospheric humidity can be found even with fixed entrainment.

(3) Associated with the smaller buoyancy in the lower free troposphere compared to the oceanic case, the role of freezing is more important to occurrences of positive buoyancy in the upper troposphere. If freezing is completely omitted, the jump in buoyancy seen near 550 mb in Fig. 9 does not occur, and profiles in the upper troposphere decrease slightly faster with height, yielding little buoyancy even in the high CWV cases.

The discussion of caveats above points to some interesting aspects in which representation of deep convection over tropical land can be expected to be more sensitive than over the ocean. The additional involvement of the boundary layer in setting deep convective instability is no surprise. However, the dependence of the deep convective instability through the upper troposphere on contributions to buoyancy from the freezing process even under highly favorable conditions in terms of free tropospheric water vapor and favorable time of day points to a potentially greater sensitivity to freezing microphysics than over ocean. This will be addressed in further work. Nonetheless, the overall results for the leading order effects of lower free tropospheric water vapor on convection in the Amazon have striking parallels to the oceanic case.

8. Conclusions

This study compares and contrasts the relationship between CWV and deep convection in the Amazon to that in the tropical western Pacific using measurements from two neighboring sites at each location: specifically, results from the GOAmazon site in Manacapuru, BR and the GNSS site at INPA in Manaus, BR are compared to results from the DOE ARM sites at Nauru and Manus Island. The relationships evident at all locations are robust, with an increase in conditionally averaged rain rate as a function of CWV. The probability of precipitation often increases beyond 50% in the highest CWV bins. The distribution of CWV is consistent with the distributions observed in microwave retrievals over ocean (Neelin et al. 2009) for both precipitating points and all points, with the distribution for precipitating points peaking just below the critical value at which precipitation increases sharply, and decreasing rapidly over the pickup region. All cases with sufficient data counts are consistent with a longer-than-Gaussian tail extending out to high CWV. Much of the variability in column moisture is due to variability in free tropospheric humidity, suggesting that the onset of deep convection is just as dependent on free tropospheric humidity at tropical land sites as it is over tropical ocean sites.

The relationship between CWV and precipitation is generally robust across time-of-day. While there is a smaller fraction of precipitating points of a given CWV in nighttime hours compared to those occurring near midday, the conditionally averaged precipitation exhibits a very comparable pickup that increases beyond a threshold value of CWV. Thus while the probability of nighttime precipitation likely depends on boundary layer factors, CWV remains an important proxy for the effects of lower free tropospheric water vapor on deep convection.

Because convection occurs at small time and space scales, spatial and temporal averaging can degrade the statistics describing the transition to deep convection. In daily averages, a highly smoothed version of the behavior may still be seen, but much information about the underlying physics - particularly the sharp onset of conditional instability associated with deep convection - is largely lost. Daily averages are thus suboptimal for examining this behavior and their use for such an analysis is not recommended. Examining these statistics at various averaging intervals closer to the appropriate time scales for convection indicates that the pickup curves are robust over averages from 15 minutes to 3 hours. One-hour averages yield results very similar to 15-minute averages, while 3-hour averages slightly reduce the sharpness of the pickup. Similarly, using satellite retrievals of precipitation for a region surrounding the GOAmazon site at different spatial resolution yields convective transition statistics that reasonably reflect the in situ observations at 0.25° resolution, but are slightly smoothed for 1.25° and 2.5° averages. At 2.5°, the sharpness of the pickup is lost.

Examining the temporal and vertical structure, lower tropospheric moisture increases prior to convection and precipitation at the GOAmazon site. This is consistent with findings for the tropical western Pacific ARM sites (Holloway and Neelin 2009). However, for the land case there are clear indications that following the convection, moisture has been lofted, likely as a result of the detrainment of water at various levels during the convective event. After convection, the sub-cloud layer becomes cooler and slightly drier over land. The before and after moisture profiles in this tropical land case thus illustrate the two-way interaction between convection and water vapor, with increases in lower tropospheric water vapor prior to convection consistent with impacts on buoyancy in entraining convection.

The latter impacts are tested by computing buoyancy profiles with a previously used profile of turbulent entrainment, which are then conditionally averaged by CWV to assess whether buoyancy through a deep convective layer is comparable to the onset of precipitation as a function of CWV. This is examined for soundings from all times of day, and for nighttime and midday ensembles of profiles separately. For nighttime conditions, the averages at each CWV value indicate significant CIN must be overcome in order to convect, although this is considerably less for the highest CWV values. The nighttime results underscore the presence of pre-existing disturbances or boundary layer conditions not captured by CWV. The midday soundings show buoyancies sufficient for shallow convection over a middle range of CWV. However, only the highest CWV bins would be convective through a deep layer for each case - nighttime, midday and all times - consistent with the pickup of precipitation. Some differences relative to the ocean are worth noting: there are likely greater contributions from the boundary layer to the conditional instability of the environment that cannot be sufficiently explained by variability in CWV, and there is evidence that freezing microphysics exerts greater influence on the development of buoyancy above the freezing level. Nevertheless, the dependence of deep convective onset on free tropospheric humidity is robust and of leading order over both tropical land and tropical ocean.

Acknowledgements

U.S. Department of Energy Atmospheric Radiation Measurement (ARM) Climate Research Facility GOAmazon and Tropical West Pacific field campaign data were essential to this work. This research was supported by the Office of Biological and Environmental Research of the U.S. Department of Energy grant DE-SC0011074, National Science Foundation Grant AGS-1102838, National Oceanic and Atmospheric Administration Grants NA14OAR4310274. We thank C. Holloway for providing analysis routines.

Appendix

To illustrate the consistency between radiometer CWV and radiosonde CWV, Fig. A1 shows 15-min average radiometer CWV scattered against radiosonde CWV. CWV is thus sampled every 6 hours within the period 10 Jan - 30 Sep 2014. It is evident that there are no systematic biases observed at high values of CWV, which could have resulted from interpolation or measurement inaccuracy. Overall, while our ability to confirm consistency between instruments is limited to the sampling of the radiosondes, it is evident from this sample that the CWV values agree well across instruments.

Figure A2 shows the probability density functions (PDFs) of the five precipitation datasets used throughout this study: AOSMET at the GOAmazon site, ORG at Nauru, ORG at Manus Island, TRMM, and the dataset from INPA in Manaus, Brazil coincident with the GPS CWV measurements. It is evident that the PDFs of the precipitation data from the GOAmazon site, Nauru, and Manus Island are all consistent with one another, whereas the TRMM and INPA datasets are biased low. This contributes to differences in the magnitudes of the pickup curves between those seen in Fig. 4 (TRMM) and Fig. 5 (INPA), in comparison to Figs. 1 and 2. The TRMM data in Fig. 4 require a unique precipitation axis to those of Figs. 1 and 2, since these data have a different spatial footprint than all others used in this study. Fig. 5, on the other hand, adopts an axis that is scaled according to the ratio of 30-minute mean INPA data and 30-minute mean radiometer data. This value (4.68 mm hr^{-1}) is divided by the range used in Figure 1d (6 mm hr^{-1}) to instead yield a range of 1.28 mm hr^{-1} for the axes in Fig. 5.

Figure A3 compares the available precipitation observing systems at the GOAmazon site by scattering the 15-minute average precipitation rates of each system against the chosen data set, AOSMET. Between 01 Jan and 15 Oct 2014, four instruments recorded precipitation: an optical rain gauge (ORG), a present weather detector (PWD), a Vaisala WXT520 from the Aerosol Observing Meteorological Station (AOSMET), and a Vaisala WXT520 from a system including a 3-channel microwave radiometer (MWR3C). Comparison to MWR3C precipitation is not included in this analysis, but the data compare well with the AOSMET precipitation chosen for use in this study (personal communication, ARM Climate Research Facility Data Quality Office).

Figure A3a shows the PWD and ORG datasets scattered against the AOSMET dataset. Two main features are worth noting: (1) the plateau of rain rates in the PWD data (blue), and (2) the erroneous rainfall measured by the ORG (green). The plateau of PWD rain rates indicates that the instrument records a maximum value of ~8-10 mm hr^{-1}; this leads to the systematic recording of erroneously low rain rates above an unknown threshold. These data could be used to confirm the incidence of rain, but analysis of the rain rate magnitudes using these data is not recommended. The ORG had many operational problems throughout the specified time period and thus often recorded precipitation when it was not raining, as is evident from the scatter on the ordinate. Less evident are all of the erroneous values at low rain rates recorded as a result of instrument malfunction. Eliminating all points < 0.5 mm hr^{-}

^{1} in the ORG data would likely remedy some issues on the low end, but a threshold would not likely help to eliminate erroneous data on the high end. Therefore, these data must be extensively examined and errors must be corrected for before using these data prior to 15 Oct 2014 when the instrument was repaired (personal communication, ARM Climate Research Facility Data Quality Office).

After 15 Oct 2014, five instruments measured precipitation at the GOAmazon site; all data besides that from the MWR3C system are included in Fig. A3b. It is evident that the ORG data are consistent with the AOSMET precipitation after 15 Oct 2014, as are the data from the Parisvel laser disdromeder (PARS) and the tipping bucket rain gauge (RAIN). Overall, however, the AOSMET precipitation data set is the most reliable for use throughout the entire GOAmazon campaign, and is thus chosen for use in this analysis. Prior to 15 Oct 2014, use of neither the PWD nor the ORG precipitation data sets is recommended.

Although the qualitative convective transition statistics are robust across a broad set of instrumentation, careful consideration must be given to the precipitation observing system for quantitative aspects, as systematic biases and instrument error could affect comparisons to model output.

References

Adams, D.K., R. Fernandes, E.R. Kursinski, J.M. Maia, L.F. Sapucci, L.A. Machado, I. Vitorello, J.F.G. Monico, K.L. Holub, S.I. Gutman, and N. Filizola, 2011: A dense GNSS meteorological network for observing deep convection in the Amazon. *Atmospheric Science Letters*, *12*, 207-212.

Adams, D. K., S. I. Gutman, K. L. Holub, and D. S. Pereira, 2013: GNSS observations of deep convective time scales in the Amazon. *Geophysical Research Letters*, **40**, 2818-2823.

Andreae, M. O., D. Rosenfeld, P. Artaxo, A. A., Costa, G. P., Frank, K. M. Longo, and M. A. F. Silva-Dias, 2004: Smoking rain clouds over the Amazon. *Science*, **303**, 1337–1342.

Austin, J. M., 1948: A note on cumulus growth in a nonsaturated environment. J. Meteor., 5, 103–107.

Bacmeister, J. T., and G. L. Stephens, 2011: Spatial statistics of likely convective clouds in CloudSat data. *JGR Atm.*, **116**, D04104 1-21.

Bechtold, P., J. Chaboureau, A. Beljaars, A. K. Betts, M. Kohler, M. J. Miller, & J. Redelsperger, 2004: The simulation of the diurnal cycle of convective precipitation over land in a global model. *Q. J. Roy. Meteor. Soc.*, **130**, 3119–3137.

Bechtold, P., M. Kohler, T. Jung, F. Doblas-Reyes, M. Leutbecher, M. J. Rodwell, F. Vitart and G. Balsamo, 2008: Advances in simulating atmospheric variability with the ECMWF model: From synoptic to decadal time-scales. *Q. J. R. Meteorol. Soc.*, **134**, 1337–1351.

Benedict, J. J., and D. A. Randall, 2007: Observed characteristics of the MJO relative to maximum rainfall. *J. Atmos. Sci.,* **64**, 2332–2354.

Betts, A. K., and C. Jakob, 2002: Study of diurnal cycle of convective precipitation over Amazonia using a single column model, *J. Geophys.Res.,* **107**, 4732.

Bevis, M., S. Businger, T. A. Herring, C. Rocken, R. A. Anthes, and R. H. Ware, 1992: GPS meteorology: Remote sensing of atmospheric water vapor using the Global Positioning System. *Journal of Geophysical Research: Atmospheres,* **97.D14**, 15787-15801.

Biasutti, M., A. H. Sobel, and Y. Kushnir, 2006: GCM precipitation biases in the Tropical Atlantic. *J. Clim.*, **19**, 935–958.

Boing, S. J., H J. J. Jonker, A. P. Siebesma, and W. W. Grabowski, 2012: Influence of the Subcloud Layer on the Development of a Deep Convective Ensemble. *J. Atmos. Sci.,* **69**, 2682-2698.

Bretherton, C. S., M. E. Peters, and L. E. Back, 2004: Relationships between water vapor path and precipitation over the tropical oceans. *J. Climate*, **17**, 1517–1528.

Brown, R. G., and C. Zhang, 1997: Variability of midtropospheric moisture and its effect on cloud-top height distribution during TOGA COARE. *J. Atmos. Sci.,* **54**, 2760–2774.

Chaboureau, J. P., F. Guichard, J. L. Redelsperger, and J. P. Lafore, 2004: The role of stability and moisture in the diurnal cycle of convection over land. *Q. J. R. Meteorol. Soc.*, **130**, 3105–3117.

Collow, A.B., M.A. Miller, and L. Trabachino, 2016: Cloudiness over the Amazon Rainforest: Meteorology and thermodynamics. *J. Geophys. Res.: Atmos.,* in revision.

Dai, A., and K. E. Trenberth, 2004: The Diurnal Cycle and Its Depiction in the Community Climate System Model. *J. Climate,* **17**, 930–951.

Dai, A., 2006: Precipitation characteristics in eighteen coupled climate models. *J. Climate*, **19**, 4605–4630.

Del Genio, A.D., and J. Wu, 2010: The Role of Entrainment in the Diurnal Cycle of Continental Convection. *J. Climate*, **23**, 2722–2738.

Del Genio A.D., Y. Chen, D. Kim, and M.-S. Yao, 2011: The MJO transition from shallow to deep convection in CloudSat/CALIPSO data and GISS GCM simulations. J. Climate

Derbyshire, S. H., I. Beau, P. Bechtold, J.-Y. Gandpeix, J.-M. Piriou, J.-L. Redelsperger, and P. Soares (2004), Sensitivity of moist convection to environmental humidity. *Q. J. R. Meteorol. Soc.,* **130**, 3055 – 3079.

Emanuel, K. A., 1994: Atmospheric Convection. 1st ed. Oxford University Press, 580 pp.

Grabowski, W. W., 2003: MJO-like coherent structures: Sensitivity simulations using the cloud-resolving convection parameterization (CRCP). *J. Atmos. Sci.,* **60**, 847–864.

Grabowski, W. W. and M. W. Moncrieff, 2004: Moisture–convection feedback in the tropics. *Q. J. R. Meteorol. Soc.,* **130**, 3081–3104.

Grabowski, W. W., 2006: Impact of explicit atmosphere–ocean coupling on MJO-like coherent structures in idealized aquaplanet simulations. *J. Atmos. Sci.,* **63**, 2289–2306.

Guichard, F., J. C. Petch, J.-L. Redelsperger P. Bechtold, J.-P. Chaboureau, S. Cheinet, W. Grabowski, H. Grenier, C. G. Jones, M. Köhler, et al., 2004: Modelling the diurnal cycle of deep precipitating convection over land with cloud-resolving models and single column models, *Q. J. R. Meteorol. Soc.,* ***130***, 3139 – 3172.

Hagos, S., Z. Feng, K. Landu, C. N. Long, 2014: Advection, moistening, and shallow-to-deep convection transitions during the initiation and propagation of Madden-Julian Oscillation. *JAMES*, **6(3)**, 938-949.

Hannah, W. M. and E. D. Maloney, 2011: The Role of Moisture–Convection Feedbacks in Simulating the Madden–Julian Oscillation. J. Climate, 24, 2754–2770.

Hirota, N., and Y. N. Takayabu, 2013: Reproducibility of precipitation distribution over the tropical oceans in CMIP5 multi-climate models compared to CMIP3. *Clim. Dyn.,* **41**, 2909–2920.

Hirota, H., Y. N. Takayabu, M. Watanabe, M. Kimoto, and M. Chikira, 2014: Role of Convective Entrainment in Spatial Distributions of and Temporal Variations in Precipitation over Tropical Oceans. *J. Clim.,* **27**, 8707–8723.

Hohenegger, C., and B. Stevens, 2013: Preconditioning Deep Convection with Cumulus Congestus. *J. Atmos. Sci.,* **70**, 448–464.

Holloway, C. E., and J. D. Neelin, 2009: Moisture Vertical Structure, Column Water Vapor, and Tropical Deep Convection. *J. Atmos. Sci.,* **66**, 1665–1683.

Holloway, C. E., and J. D. Neelin, 2010: Temporal Relations of Column Water Vapor and Tropical Precipitation. *J. Atmos. Sci.,* **67**, 1091–1105.

Holloway, C. E., S. J. Woolnough, and G. M. S. Lister, 2013: The Effects of Explicit versus Parameterized Convection on the MJO in a Large-Domain High-Resolution Tropical Case Study. Part I: Characterization of Large-Scale Organization and Propagation. *J. Atmos. Sci.,* **70**, 1342–1369.

Jensen, M. P., and A. D. Del Genio, 2006: Factors Limiting Convective Cloud-Top Height at the ARM Nauru Island Climate Research Facility. *J. Clim.,* **19**, 2105-2117.

Jiang, X., D. E. Waliser, W. S. Olson, W. K. Tao, T. S. L'Ecuyer, , K. F. Li, Y. L. Yung, S. Shige, S. Lang, and Y. N. Takayabu, 2011: Vertical diabatic heating structure of the MJO: Intercomparison between recent reanalyses and TRMM estimates. *Monthly Weather Review*, **139**, 3208-3223.

Johnson, R. H., T. M. Rickenbach, S. A. Rutledge, P. E. Ciesielski, and W. H. Schubert, 1999: Trimodal characteristics of tropical convection. *J. Clim.,* **12**, 2397–2418.

Kemball-Cook, S. R., and B. C. Weare, 2001: The onset of convection in the Madden-Julian oscillation. *J. Clim.,* **14**, 780–793.

Khairoutdinov, M., and D. Randall, 2006: High-resolution simulation of shallow-to-deep convection transition over land, *J. Atmos. Sci.,* **63**, 3421 – 3436.

Kim, D., A. H. Sobel, A. D. Del Genio, Y. Chen, S. J. Camargo, M.-S. Yao, M. Kelley, and L. Nazarenko, 2012: The Tropical Subseasonal Variability Simulated in the NASA GISS General Circulation Model. *J. Climate*, **25**, 4641–4659.

Khain, A., D. Rosenfeld, and A. Pokrovsky, 2005: Aerosol impact on the dynamics and microphysics of deep convective clouds. *Q. J. R. Meteorol. Soc.*, **131**, 2639–2663.

Kim, D., P. Xavier, E. Maloney, M. Wheeler, D. Waliser, K. Sperber, H. Hendon, C. Zhang, R. Neale, Y.-T. Hwang, H. Liu, 2014: Process-Oriented MJO Simulation Diagnostic: Moisture Sensitivity of Simulated Convection. *Journal of Climate,* **27**, 5379-5395.

Kuang, Z., and C. S. Bretherton 2006: A mass-flux scheme view of a high-resolution simulation of a transition from shallow to deep convection, *J. Atmos. Sci.*, **63**, 1895 – 1909.

Kumar, V. V., C. Jakob, A. Protat, P. T. May, and L. Davies, 2013: The four cumulus cloud modes and their progression during rainfall events: AC-band polarimetric radar perspective. *J. Geophys. Res. Atmos.,* **118**, 8375–8389.

Kummerow, C., Y. Hong, W. S. Olson, S. Yang, R. F. Adler, J. McCollum, R. Ferraro, G. Petty, Dong-Bin Shin, and T. T. Wilheit, 2001: The evolution of the Goddard Profiling Algorithm (GPROF) for rainfall estimation from passive microwave sensors. *Journal of Applied Meteorology,* **40**, 1801-1820.

LeMone, M. A., E. J. Zipser, and S. B. Trier, 1998: The Role of Environmental Shear and Thermodynamic Conditions in Determining the Structure and Evolution of Mesoscale Convective Systems during TOGA COARE. *J. Atmos. Sci.,* **55**, 3493–3518.

Lintner, B. R., and J. D. Neelin, 2007: A prototype for convective margin shifts. *Geophysical Research Letters,* **34**, L05812.

Lintner, B. R., and J. D. Neelin, 2008: Eastern margin variability of the South Pacific convergence zone. *Geophys. Res. Lett.,* **35**, L16701.
Lintner, B.R., and J.D. Neelin, 2009: Soil moisture impacts on convective margins. *J. Hydrometeor*., **10**, 1026—1039.
Lintner, B.R., and J. D. Neelin, 2010: Tropical South America–Atlantic Sector Convective Margins and Their Relationship to Low-Level Inflow. *Journal of Climate,* **23**, 10, 2671-2685.
Luo, Z. J., G. Y. Liu, and G. L. Stephens, 2010: Use of A-train data to estimate convective buoyancy and entrainment. *Geophys. Res. Lett.,* **37**, L09804.
Ma, H-Y., X. Ji, J. D. Neelin, and C. R. Mechoso, 2011: Mechanisms for Precipitation Variability of the Eastern Brazil/SACZ Convective Margin, *Journal of Climate*, **24**, 13, 3445-3456.
Malkus, J. S., 1954: Some results of a trade-cumulus cloud investigation. *J. Meteor.*, **11**, 220–237.
Mapes, B., S. Tulich, J. Lin, and P. Zuidema, 2006: The mesoscale convection life cycle: Building block or prototype for largescale tropical waves? *Dyn. Atmos. Oceans,* **42**, 3–29.
Masunaga, H., 2013: A satellite study of tropical moist convection and environmental variability: A moisture and thermal budget analysis. *J. Atmos. Sci.,* **70**, 2443–2466.
Morris, V.R., 2006: Microwave radiometer (MWR) handbook. *ARM-TR016*.
Neale, R. B., J. H. Richter, and M. Jochum, 2008: The impact of convection on ENSO: From a delayed oscillator to a series of events. *J. Climate*, **21**, 5904-5924.
Neelin, J. D., and I. M. Held, 1987: Modeling tropical convergence based on the moist static energy budget. *Monthly Weather Review,* **115**, 3-12.
Neelin, J.D., O. Peters, and K. Hales, 2009: The Transition to Strong Convection. *J. Atmos. Sci.,* **66**, 2367–2384.
Neelin, J.D., B.R. Lintner, B. Tian, Q.B. Li, L. Zhang, P.K. Patra, M.T. Chahine, and S.N. Stechmann, 2010: Long tails in deep columns of natural and anthropogenic tracers. *Geophys. Res. Lett.,* **37**, L05804.
Nesbitt, S. W., and E. J. Zipser, 2003: The diurnal cycle of rainfall and convective intensity according to three years of TRMM measurements. *J. Climate*, **16**, 1456–1475.
Oueslati, B., and G. Bellon, 2013: Convective Entrainment and Large-Scale Organization of Tropical Precipitation: Sensitivity of the CNRM-CM5 Hierarchy of Models. *J. Clim.,* **26**, 2931–2946.
Parsons, D. B., K. Yoneyama, and J.-L. Redelsperger, 2000: The evolution of the tropical western Pacific atmosphere–ocean system following the arrival of a dry intrusion. Quart. *J. Roy. Meteor. Soc.,* **126**, 517–548.
Peters, O., and J. D. Neelin, 2006: Critical phenomena in atmospheric precipitation. *Nature Phys.,* **2**, 393–396.
Randall, D. A., Harshvardhan, and D. A. Dazlich, 1991: Diurnal variability of the hydrologic cycle in a general circulation model. *J. Atmos. Sci.,* **48**, 40–62.
Raymond, D. J. and A. M. Blyth, 1986: A stochastic mixing model for nonprecipitating cumulus clouds. *J. Atmos. Sci.,* **43**, 2708-2718.

Raymond, D. J. and D. J. Torres, 1998: Fundamental moist modes of the equatorial troposphere. *J. Atmos. Sci.,* **55**, 1771-1790.

Raymond, D. J., 2000: Thermodynamic control of tropical rainfall. *Quart. J. Roy. Meteor. Soc.,* **126**, 889–898.

Raymond, D. J. and X. Zeng, 2000: Instability and large-scale circulations in a two-column model of the tropical troposphere. *Quart. J. Roy. Meteor. Soc.,* **126**, 3117-3135.

Raymond, D. J., S. L. Sessions, A. H. Sobel, and Z. Fuchs, 2009: The Mechanics of Gross Moist Stability. *JAMES*, **1**, Art. 9.

Redelsperger, J. L., D. B. Parsons, and F. Guichard, 2002: Recovery processes and factors limiting cloud-top height following the arrival of a dry intrusion observed during TOGA–COARE. *J. Atmos. Sci.,* **59**, 2438–2457.

Ridout, J., 2002: Sensitivity of Tropical Pacific Convection to Dry Layers at Mid-to Upper Levels: Simulation and Parameterization Tests. J. Atmos. Sci., 59, 3362-3381.

Romps, D. M., and Z. Kuang, 2010: Do Undiluted Convective Plumes Exist in the Upper Tropical Troposphere? J. Atmos. Sci., 67, 468-484.

Rotunno, R., J. B. Klemp, and M. L. Weisman, 1988: A Theory for Strong, Long-Lived Squall Lines. *J. Atmos. Sci.,* **45**, 463–485.

Rowe, A. K., and R. A. Houze, Jr., 2015: Cloud organization and growth during the transition from suppressed to active MJO conditions. *J. Geophys. Res. Atmos.*, **120**, 10324–10350.

Sahany, S., J. D. Neelin, K. Hales, and R. B. Neale, 2012: Temperature-moisture dependence of the deep convective transition as a constraint on entrainment in climate models. *J. Atmos. Sci.,* **69**, 1340–1358.

Sahany, S., J. D. Neelin, K. Hales and R. B. Neale, 2014: Deep Convective Transition Characteristics in the NCAR CCSM and Changes Under Global Warming. *J. Climate*, **27**, 9214-9232.

Schlemmer, L., and C. Hohenegger, 2014: The Formation of Wider and Deeper Clouds as a Result of Cold-Pool Dynamics. *J. Atmos. Sci.,* **71**, 2842–2858.

Sherwood, S. C., and R. Wahrlich, 1999: Observed evolution of tropical deep convective events and their environment. *Mon. Wea. Rev.,* **127**, 1777–1795.

Sherwood, S. C., P. Minnis, and M. McGill, 2004: Deep convective cloud-top heights and their thermodynamic control during CRYSTAL–FACE. *J. Geophys. Res.*, **109**, D20119.

Siebesma, A. P., P. M. M. Soares, and J. Teixeira, 2007: A combined eddy-diffusivity mass-flux approach for the convective boundary layer. *J. Atmos. Sci.,* **64**, 1230–1248.

Simpson, J., 1971: On cumulus entrainment and one-dimensional models. *J. Atmos. Sci.,* **28**, 449-455.

Sobel, A. H., S. E. Yuter, C. S. Bretherton, and G. N. Kiladis, 2004: Large-Scale Meteorology and Deep Convection during TRMM KWAJEX. *Monthly Weather Review*, **132**, 422-444.

Stechmann, S. N., and J. D. Neelin, 2011: A stochastic model for the transition to strong convection. *J. Atmos. Sci.*, **68**, 2955–2970.

Stechmann, S. N., and J. D. Neelin, 2014: First-Passage-Time prototypes for precipitation statistics. *J. Atmos. Sci.,* **71**, 3269-3291.
Stirling, A. J., and R. A. Stratton, 2012: Entrainment processes in the diurnal cycle of deep convection over land. *Q. J. R. Meteorol. Soc.,* **138**, 1135 – 1149.
Tian, B., D. Waliser, E. J. Fetzer, B. H. Lambrigtsen, Y. L. Yung, and B. Wang, 2006: Vertical most thermodynamic structure and spatial-temporal evolution of the MJO in AIRS observations. *J. Atmos. Sci.,* **63**, 2462-2485.
Tompkins, A. M., 2001a: Organization of tropical convection in low vertical wind shears: The role of water vapor. *J. Atmos. Sci.,* **58**, 529–545.
Tompkins, A. M., 2001b: Organization of tropical convection in low vertical wind shears: The role of cold pools. *J. Atmos. Sci.,* **58**, 1650–1672
Waite, M. L., and B. Khouider, 2010: The deepening of tropical convection by congestus preconditioning*. J. Atmos. Sci.,* **67**, 2601–2615.
Wei, D., A. M. Blyth, and D. J. Raymond, 1998: Buoyancy of convective clouds in TOGA COARE. *J. Atmos. Sci.,* **55**, 3381–3391.
Wu, C.-M., B. Stevens, and A. Arakawa, 2009: What controls the transition from shallow to deep convection? *J. Atmos. Sci*., **66**, 1793-1806.
Yang, G. Y., and J. M. Slingo, 2001: The diurnal cycle in the tropics, *Mon. Weather Rev.,* **129**, 784 – 801.
Yoneyama, K. and T. Fujitani, 1995: The behavior of dry westerly air associated with convection observed during the TOGA-COARE R/V Natsushima cruise. *Journal-Meteorological Society of Japan*, **73**, 291-304.
Zhang Y., and Klein S. A., 2010: Mechanisms affecting the transition from shallow to deep convection over land: Inferences from observations of the diurnal cycle collected at the ARM Southern Great Plains Site. *J. Atmos. Sci.,* **67**, 2943–2959.
Zhao, M., I. M. Held, S.-J. Lin, And G. A. Vecchi, 2009: Simulations of Global Hurricane Climatology, Interannual Variability, and Response to Global Warming Using a 50-km Resolution GCM. *J. Climate*, **22**, 6653-6678.

Figure Captions

Figure 1: The relationship between precipitation and CWV at the GOAmazon site in Manacapuru, BR. (a) The 1-hour average precipitation (mm hr^{-1}) centered at the time of radiosonde launch conditionally averaged on CWV (mm). The mean of precipitating points greater than 0.1 mm hr^{-1} is 2.72 mm, given by the black triangle on the y-axis. (b) The fraction of observations per CWV bin with rain rates greater than 0.5 mm hr^{-1}, for radiosonde CWV. (c) The frequency density of all points and precipitating points with rain rates greater than 0.5 mm hr^{-1}, for radiosonde CWV. (d-f) Same as (a-c), except using 15-min average CWV from the microwave radiometer (MWR). The CWV bins for each set of analysis are given by their respective color bars. The highest bin for the radiosonde analysis has a width of 6 mm and a range from 64 mm to 70 mm, differing slightly from that of the radiometer data.

Figure 2: Same as Fig. 1, but for the relationship between precipitation and radiosonde CWV at Nauru (a-c) and Manus Island (d-f) in the tropical western Pacific. The mean of precipitating points greater than 0.1 mm hr^{-1} is 2.18 mm hr^{-1} for Nauru and 2.78 mm hr^{-1} for Manus Island. CWV bins are the same as in Fig. 1d-f (see color bar).

Figure 3: Same as Fig. 1d-f, using in-situ precipitation and radiometer CWV from the GOAmazon site, but with additional averaging intervals: 15-min averages (blue); 1-hr averages (green); 3-hr averages (yellow); daily averages (red).

Figure 4: Same as Fig. 1d-f, but instead using area-averaged TRMM 3B42 3-hourly instantaneous precipitation at varying resolution from the grid box that includes the GOAmazon site; CWV values are derived from the 15-min averages of MWR data surrounding the TRMM snapshot. (a-c) for precipitation at 0.25^o x 0.25^o horizontal resolution (grid box over GOAmazon site); (d-f) spatial average of precipitation at 1.25^o x 1.25^o around GOAmazon site ; (g-i) same as (d-f) but for 2.5^o x 2.5^o.

Figure 5: Same as Fig. 1a-c, but using in-situ precipitation (30-min averages) binned by 30-min GPS-retrieved CWV from a site at the INPA in Manaus, BR. The triangle in (a) denotes the mean of precipitating points > 0.1 mm hr^{-1}, which is 1.04 mm hr^{-1}. Note the change in the precipitation axis in comparison to Fig. 1a,d and the change in threshold value used in Fig. 5b,c. The rain gauge at the INPA is biased low (see Appendix A), and thus to allow for direct comparison to the GOAmazon case, the range on the precipitation axis defined in Fig. 1a,d (0 – 6 mm) is decreased here by a factor of 4.68, the ratio of the means between the AOSMET gauge and the INPA gauge.

Figure 6: Vertical profiles of (a) specific humidity (g kg^{-1}), (b) relative humidity (%), and (c) equivalent potential temperature (K) measured or derived from radiosonde data collected at the GOAmazon site and conditionally averaged by CWV (mm). The mean saturated equivalent potential temperature (Θ_{es}) for profiles greater than 50 mm is shown in the dashed line in (c).

Figure 7: Profiles of specific humidity differences (g kg^{-1}) from radiosonde measurements at the GOAmazon site between precipitation events (1-hour average rain rates > 0.5 mm hr^{-1}) and no precipitation events (1-hour average rain rates < 0.01 mm hr^{-1}) for 1.5-3 hours leading precipitation (red), within the

hour of precipitation (black), and 1.5-3 hours lagging precipitation (blue). Results are shown for Jan-Apr only (2014-2015).

Figure 8: Same as Fig. 1d-f, except for (a-c) nighttime hours (8 pm – 7 am), and (d-f) midday hours (10 am – 4 pm) only.

Figure 9: Virtual temperature (T_v) difference between the parcel (computed with turbulent entrainment) and the environment, binned by CWV. CWV bins are 1.5 mm in width (shown in the colorbar), with the highest bin spanning 64-70 mm and the lowest bin spanning 30-41.5 mm. Plume buoyancy differences are shown in (a) for all times of day, (b) for nighttime soundings (19:30, 01:30, 07:30 LST) soundings only, and (c) for midday (10:30, 13:30 LST) soundings only.

Figure A1: The relationship between radiometer CWV and radiosonde CWV for 10 Jan 2014 – 31 Jul 2014. The correlation coefficient (R) is 0.91.

Figure A2: (a) PDF of 1-min average precipitation for all five instruments used in this study. The means of precipitating points (> 0.1 mm hr^{-1}) are shown on the precipitation axis and are as follows: 7.7 mm hr^{-1} at Nauru, 9.7 at the GOAmazon site, 8.7 mm hr^{-1} at Manus Island, 2.5 mm hr^{-1} at INPA in Manaus, and 2.2 mm hr^{-1} for the TRMM 0.25^o x 0.25^o box which includes the GOAmazon site.

Figure A3: Scatterplots of the precipitation data available from various instruments at the GOAmazon site – optical rain gauge (ORG), present weather detector (PWD), Parisvel laser disdromeder (PARS), tipping bucket rain gauge (RAIN) - in comparison to the AOSMET instrument chosen for this analysis. Results shown are for the time periods (a) prior to 15 Oct 2014 (ORG and PWD only) and (b) after 15 Oct 2014, as a limited selection of reliable observations were available before 15 Oct 2014.

Figures

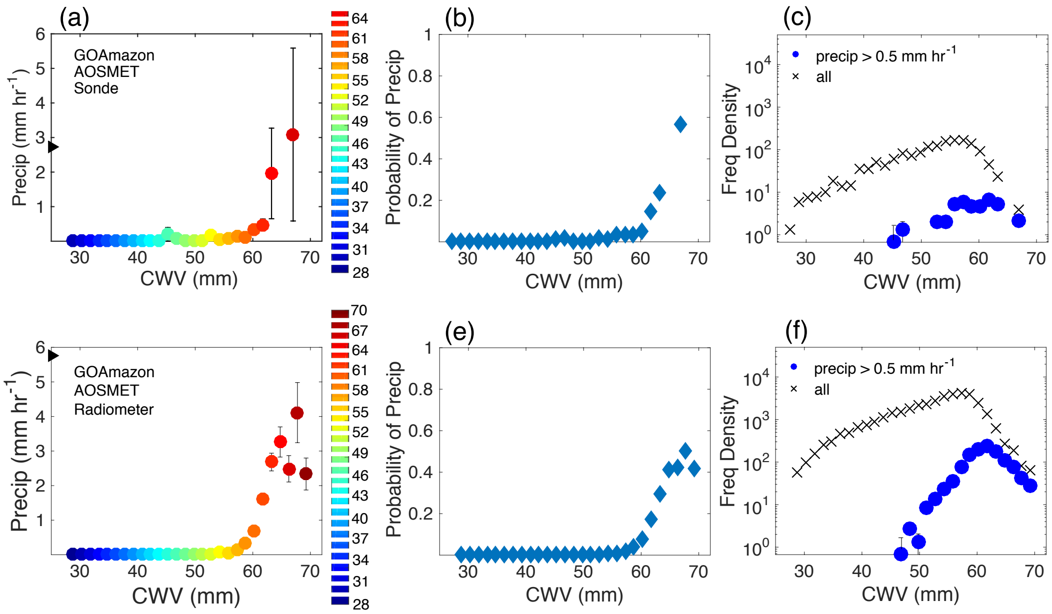

Figure 1: The relationship between precipitation and CWV at the GOAmazon site in Manacapuru, BR. (a) The 1-hour average precipitation (mm hr^{-1}) centered at the time of radiosonde launch conditionally averaged on CWV (mm). The mean of precipitating points greater than 0.1 mm hr^{-1} is 2.72 mm, given by the black triangle on the y-axis. (b) The fraction of observations per CWV bin with rain rates greater than 0.5 mm hr^{-1}, for radiosonde CWV. (c) The frequency density of all points and precipitating points with rain rates greater than 0.5 mm hr^{-1}, for radiosonde CWV. (d-f) Same as (a-c), except using 15-min average CWV from the microwave radiometer (MWR). The CWV bins for each set of analysis are given by their respective color bars. The highest bin for the radiosonde analysis has a width of 6 mm and a range from 64 mm to 70 mm, differing slightly from that of the radiometer data.

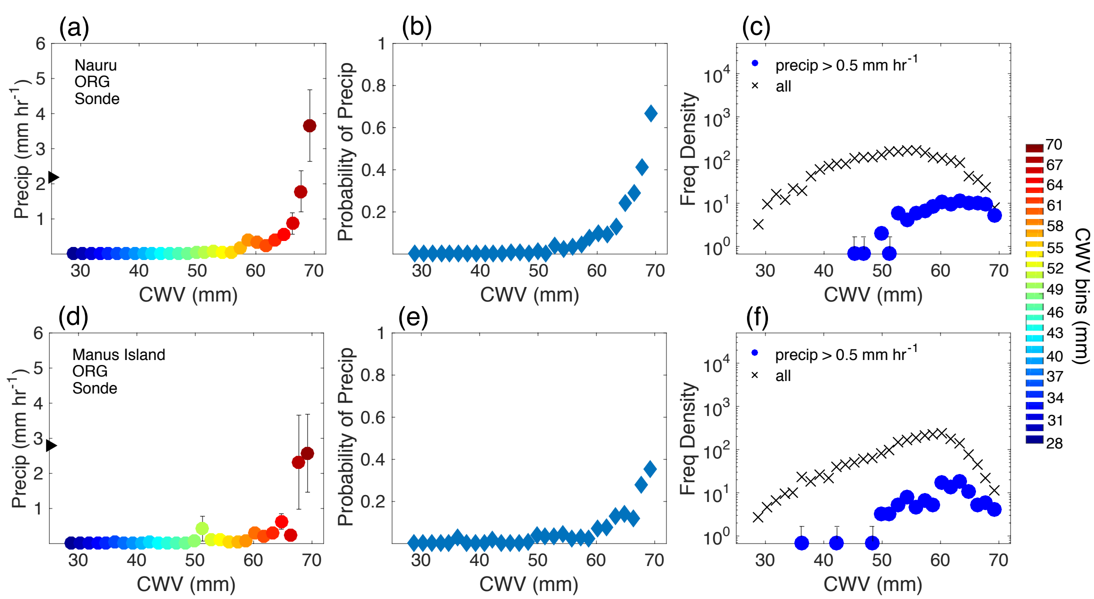

Figure 2: Same as Fig. 1, but for the relationship between precipitation and radiosonde CWV at Nauru (a-c) and Manus Island (d-f) in the tropical western Pacific. The mean of precipitating points greater than 0.1 mm hr^{-1} is 2.18 mm hr^{-1} for Nauru and 2.78 mm hr^{-1} for Manus Island. CWV bins are the same as in Fig. 1d-f (see color bar).

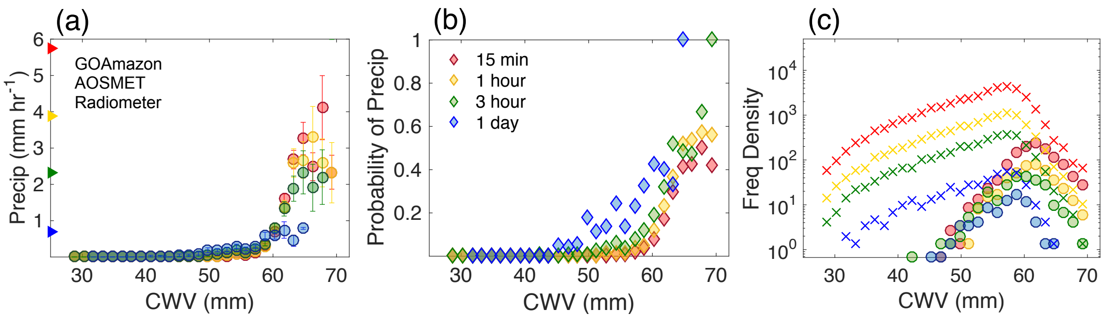

Figure 3: Same as Fig. 1d-f, using in-situ precipitation and radiometer CWV from the GOAmazon site, but with additional averaging intervals: 15-min averages (blue); 1-hr averages (green); 3-hr averages (yellow); daily averages (red).

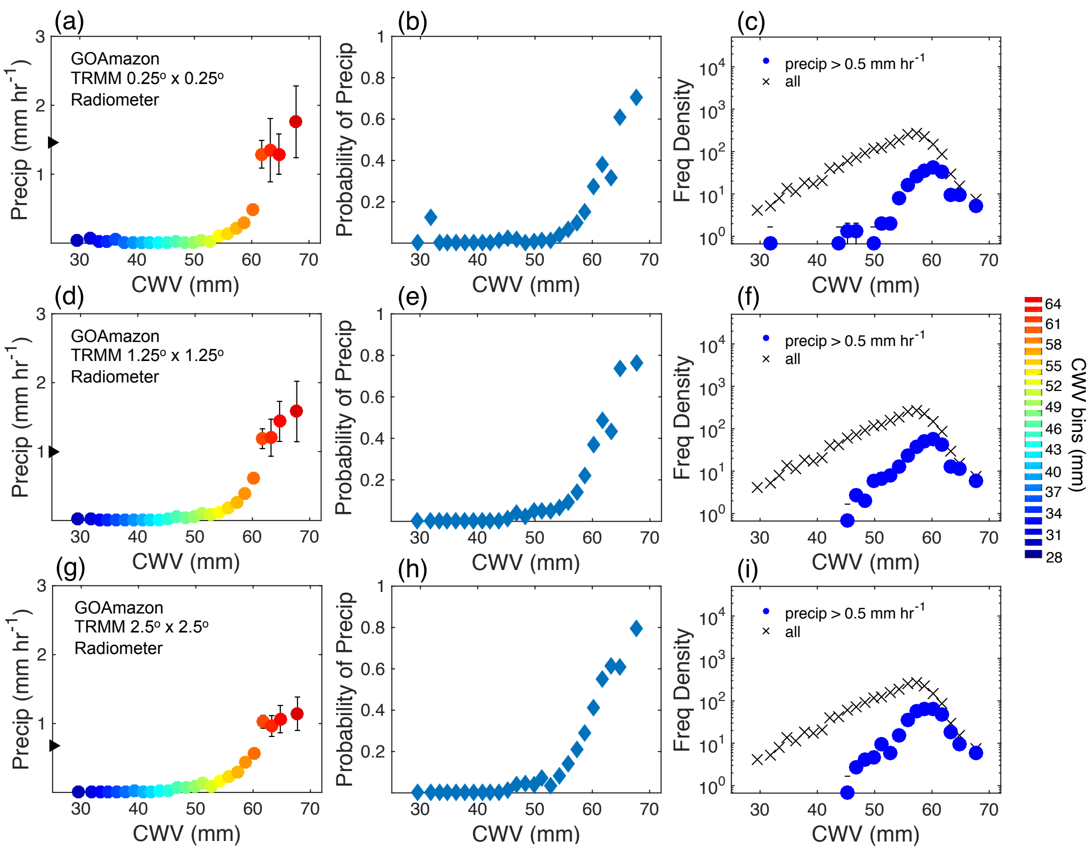

Figure 4: Same as Fig. 1d-f, but instead using area-averaged TRMM 3B42 3-hourly instantaneous precipitation at varying resolution from the grid box that includes the GOAmazon site; CWV values are derived from the 15-min averages of MWR data surrounding the TRMM snapshot. (a-c) for precipitation at 0.25º x 0.25º horizontal resolution (grid box over GOAmazon site); (d-f) spatial average of precipitation at 1.25º x 1.25º around GOAmazon site ; (g-i) same as (d-f) but for 2.5º x 2.5º.

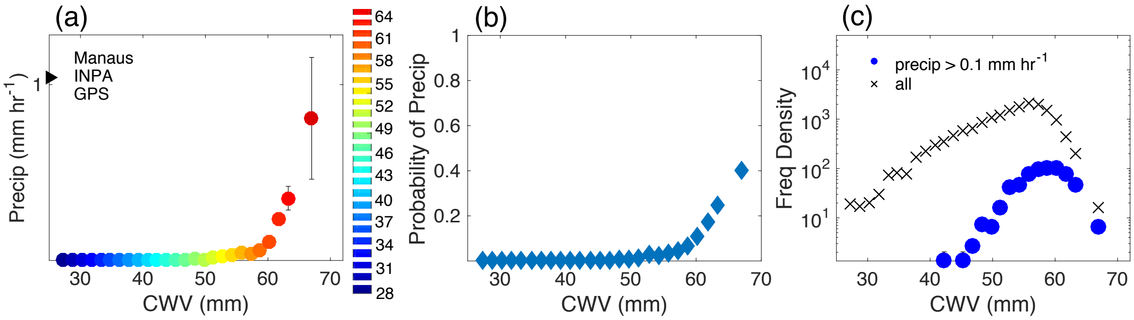

Figure 5: Same as Fig. 1a-c, but using in-situ precipitation (30-min averages) binned by 30-min GPS-retrieved CWV from a site at the INPA in Manaus, BR. The triangle in (a) denotes the mean of precipitating points > 0.1 mm hr^{-1}, which is 1.04 mm hr^{-1}. Note the change in the precipitation axis in comparison to Fig. 1a,d and the change in threshold value used in Fig. 5b,c. The rain gauge at the INPA is biased low (see Appendix A), and thus to allow for direct comparison to the GOAmazon case, the range on the precipitation axis defined in Fig. 1a,d (0 – 6 mm) is decreased here by a factor of 4.68, the ratio of the means between the AOSMET gauge and the INPA gauge.

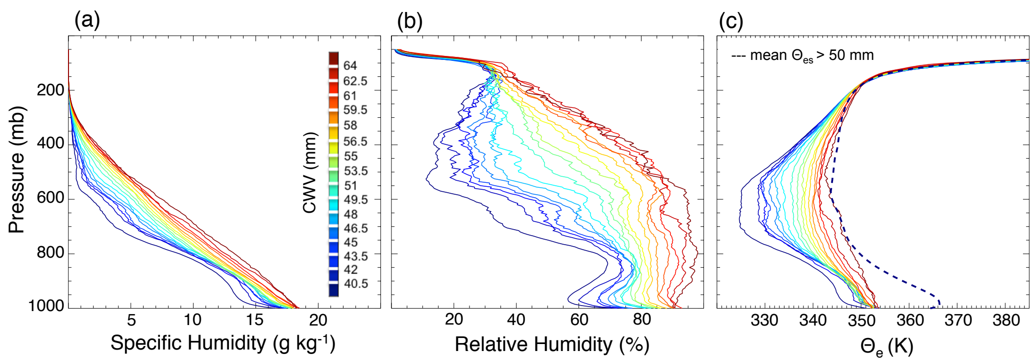

Figure 6: Vertical profiles of (a) specific humidity (g kg^{-1}), (b) relative humidity (%), and (c) equivalent potential temperature (K) measured or derived from radiosonde data collected at the GOAmazon site and conditionally averaged by CWV (mm). The mean saturated equivalent potential temperature (Θ_{es}) for profiles greater than 50 mm is shown in the dashed line in (c).

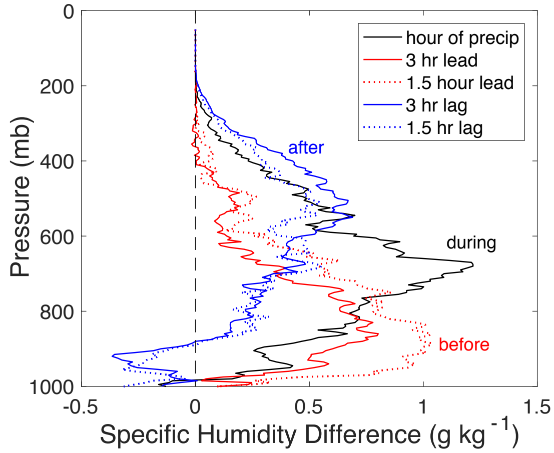

Figure 7: Profiles of specific humidity differences (g kg^{-1}) from radiosonde measurements at the GOAmazon site between precipitation events (1-hour average rain rates > 0.5 mm hr^{-1}) and no precipitation events (1-hour average rain rates < 0.01 mm hr^{-1}) for 1.5-3 hours leading precipitation (red), within the hour of precipitation (black), and 1.5-3 hours lagging precipitation (blue). Results are shown for Jan-Apr only (2014-2015).

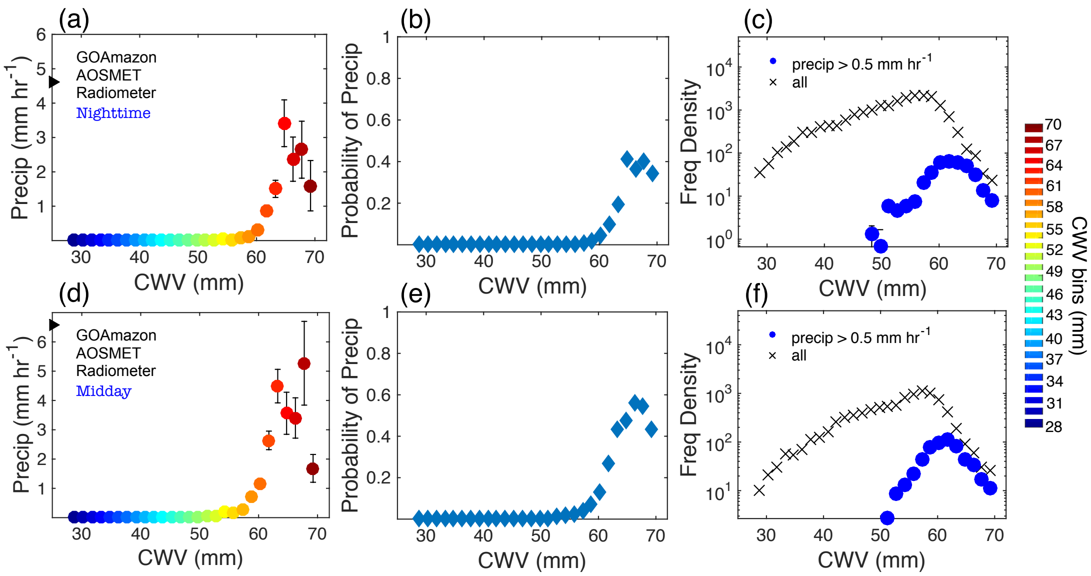

Figure 8: Same as Fig. 1d-f, except for (a-c) nighttime hours (8 pm – 7 am), and (d-f) midday hours (10 am – 4 pm) only.

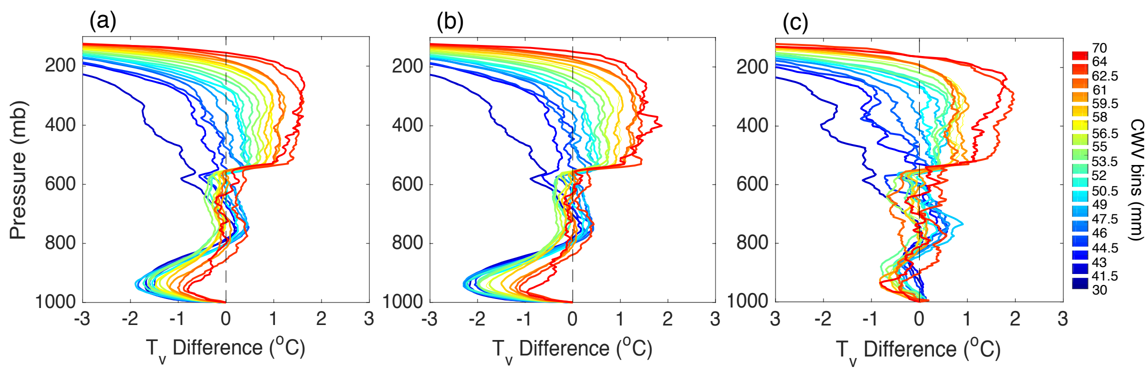

Figure 9: Virtual temperature (T_v) difference between the parcel (computed with turbulent entrainment) and the environment, binned by CWV. CWV bins are 1.5 mm in width (shown in the colorbar), with the highest bin spanning 64-70 mm and the lowest bin spanning 30-41.5 mm. Plume buoyancy differences are shown in (a) for all times of day, (b) for nighttime soundings (19:30, 01:30, 07:30 LST) soundings only, and (c) for midday (10:30, 13:30 LST) soundings only.

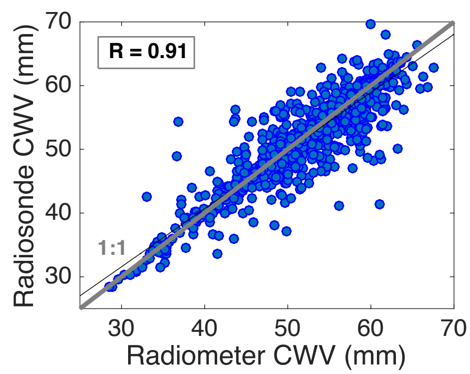

Figure A1: The relationship between radiometer CWV and radiosonde CWV for 10 Jan 2014 – 31 Jul 2014. The correlation coefficient (R) is 0.91.

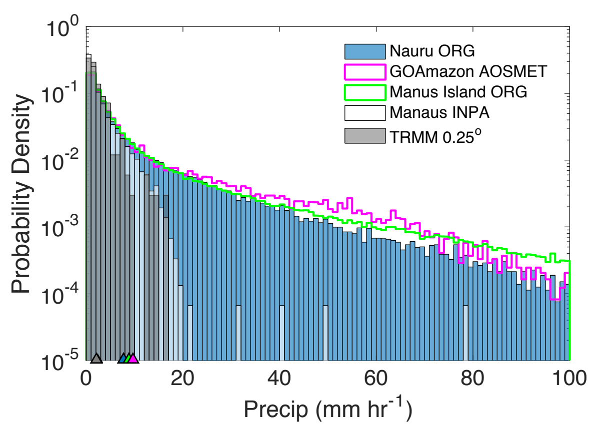

Figure A2: (a) PDF of 1-min average precipitation for all five instruments used in this study. The means of precipitating points (> 0.1 mm hr^{-1}) are shown on the precipitation axis and are as follows: 7.7 mm hr^{-1} at Nauru, 9.7 at the GOAmazon site, 8.7 mm hr^{-1} at Manus Island, 2.5 mm hr^{-1} at INPA in Manaus, and 2.2 mm hr^{-1} for the TRMM 0.25^{o} x 0.25^{o} box which includes the GOAmazon site.

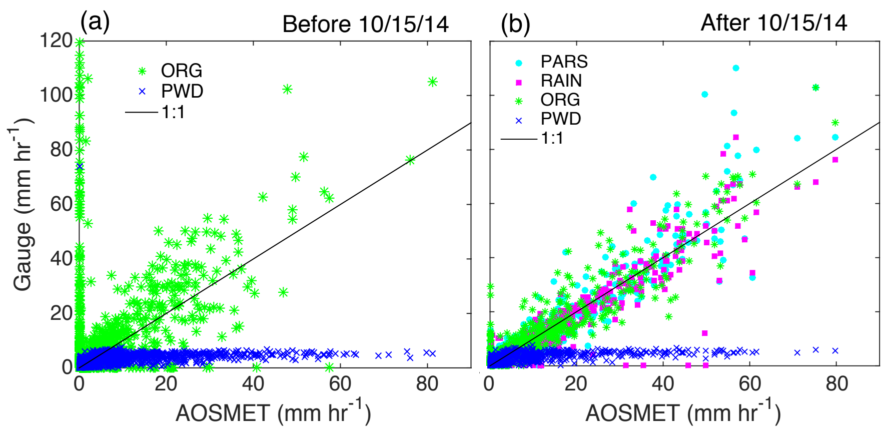

1207 **Figure A3:** Scatterplots of the precipitation data available from various instruments at the GOAmazon site – optical rain gauge (ORG), present weather detector (PWD), Parisvel laser disdromeder (PARS), tipping bucket rain gauge (RAIN) - in comparison to the AOSMET instrument chosen for this analysis. Results shown are for the time periods (a) prior to 15 Oct 2014 and (b) after 15 Oct 2014, as a limited selection of reliable observations were available before 15 Oct 2014.

1208